THERMAL MODELING OF 304L STAINLESS STEEL SELECTIVE LASER MELTING

Lan Li, Cody Lough, Adriane Replogle, Doug Bristow, Robert Landers, and Edward Kinzel

Department of Mechanical and Aerospace Engineering, Missouri University of Science and Technology, Rolla, MO 65409

Abstract

This paper describes the continuum thermal modeling of the Selective Laser Melting (SLM) process for 304L stainless steel using Abaqus. Temperature dependent thermal properties are obtained from literature and incorporated into the model capturing the change from powder to fully dense stainless steel. The thermal model predicts the temperature history for multi-track scans under different process parameters (laser power, effective scanning speed, hatch spacing) which is used to extract the melt-pool size, solidification rate, and temperature gradients. These are compared to experimental results obtained from a Renishaw AM250 in terms of the melt pool size, grain structure, and cell spacing. These experimental results are used to tune unknown simulation parameters required by the continuum model including the optical penetration depth and thermal conductivity multiplier for the molten region. This allows the model to yield predictive simulations of melt pool size and solidification structure of SLM 304L stainless steel.

1. Introduction

Selective Laser Melting (SLM) is a powder bed-based Additive Manufacturing (AM) technology. It is widely used in freeform fabrication of complex three-dimensional metal parts directly from CAD models by adding material layer by layer [1]. SLM introduces the opportunity to build parts with engineered mechanical properties. These properties are determined by the microstructure which results from part thermal processing history. Therefore, in order to produce parts with engineered properties it is critical to understand how SLM process parameters such as laser spot size, power, scanning speed, and scanning strategy determine the thermal behavior and microstructure. However, it is time-consuming and costly through experiments for detailed investigations to analyze the effect of different process parameters on the temperature distribution, solidification behavior and mechanical properties of parts. This problem can be approached by developing a numerical model to analyze all behaviors in the SLM process and understand how process parameters relate to the thermal history and ultimately engineering properties.

Recently, numerical models have been developed and used in previous studies analyzing SLM thermal mechanisms. Most of them focused on the investigation of effect of process parameters such as laser power, scanning speed, beam size and scan strategy on melt pool geometry characteristics. For instance, researchers [2-5] simulated the temperature distribution during SLM processing of 316L stainless steel. Results showed process parameters including scan speed, powder layer thickness, and thermal properties of the materials can highly affect the SLM process. In Loh et al.'s [6] investigation, the type of laser beam distributions, such as uniform and Gaussian laser distribution can highly affected the melt width and depth in SLM of aluminum alloy 6061 (AA6061). Antony et al. [7] performed numerical and experimental work on laser melting of

316L stainless steel powder on top of a 316L stainless steel substrate. They concluded that the scanning speed has no influence on track height and contact angle, while laser power and scanning speed have obvious effects on track smoothness, distortion and irregularities. These characteristics of the melt zone were in consist with experimental results. Kolossov et al. [8] developed a 3D finite element model to predict the thermal behavior on the top surface of a titanium powder bed during the SLM process. Their results showed that the thermal conductivity highly affects thermal process development. Parry et al. [9] used a thermo-mechanical model to determine the temperature history and residual stress resulting from SLM. Findings include laser scan strategies affect the stress distribution by influencing thermal history during scanning.

Regardless of these numerical simulations of the SLM process with metal powder, few researches focused on thermal behavior during SLM of 304L stainless steel powder. In this paper, a three-dimensional model is developed to predict the temperature history and microstructure parameters in the SLM process using 304L stainless steel. Abaqus FEA is used to solve these problems. This model takes latent heat of fusion as well as temperature-dependent 304L thermal properties into account. The temperature distribution, melt pool sizes and microstructure parameters and the effects of process parameters, such as laser power, scanning speed and hatch spacing are analyzed. Furthermore, experiments were conducted to study the melt pool sizes and microstructural features of SLM-produced parts using different laser processing parameters to verify the reliability of this model.

2. Numerical Analysis of Selective Laser Melting 304L Stainless Steel

2.1. Model Setup

The three-dimensional numerical modeling domain was setup as a powder bed of 304L stainless steel with dimensions of 1.4×1×0.05 mm^3 on a solid 304L substrate with dimensions of 1.4×1×0.35 mm^3 (Fig. 1). To reduce computational time, the elements interacting with the laser beam were finely meshed with hexahedral element sizes of 20 μm and a coarser mesh for the surrounding loose powder and substrate. In order to make the complicated problem mathematically tractable, the whole powder bed is considered to be a homogeneous and continuous media.

During the SLM process, the laser energy on the powder bed can be regarded as a volumetric energy density, which obeys the Gaussian heat source distribution. The most common beam profile in the laser material processing is the Gaussian distribution of energy as a volumetric heat source given by:

$$q_1 = \frac{2(1-R)P}{\pi {r_0}^2 d} \exp\left[-2\frac{r^2}{{r_0}^2}\right] \exp\left[-\frac{z}{d}\right] \quad (1)$$

where P is the laser power, r_0 is the laser radius, d is the optical penetration depth, h is the powder layer thickness. Eq.1 creates an exponentially decaying volumetric heat generation through a Gaussian distribution in the (x, y) plane and an additional decay term in the z direction.

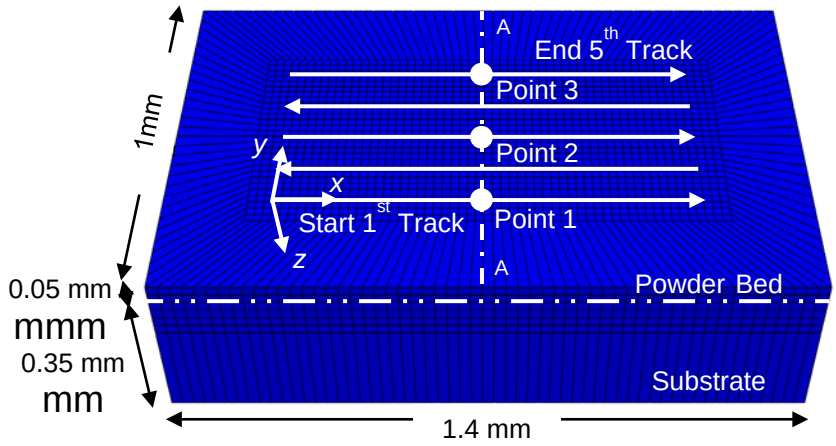

Fig. 1. FEA model geometry.

The initial condition throughout the whole powder bed and substrate is considered as uniform temperature distribution:

$$T(x,y,z,t)_{t=0} = T_0 = 353\ K \tag{2}$$

where T_0 is the ambient temperature.

Boundary conditions on the top surface of the powder bed include radiation, convection and the imposed laser heat flux. Boundary conditions are expressed as:

$$q = -k\frac{\partial T}{\partial z} + h(T - T_0) + \varepsilon\sigma(T^4 - T_0^4) \tag{3}$$

where T is temperature, h is the heat transfer coefficient of natural thermal convection of 10 W/m^2·K, σ is the Stefan-Boltzmann constant of 5.67 × 10^{-8} W/m^2·K^4 and ε is the powder bed emissivity of 0.3. Other process parameters of simulation model of 304L stainless steel are shown in Table 1.

Table 1. Hatch parameters of the simulation model.

Hatch Parameters	Model
Power, *P* [W]	120, 140, 160,180, 200
Hatch spacing, *H* [µm]	65, 105
Point distance, *pd* [µm]	50
Laser exposure time, t_e [µs]	70
Effective scan speed, *SS* [mm/s]	715
Laser Diameter, *D* [µm]	140
Optical penetration depth, *d* [µm]	50
Reflectance of SS304L, *R*	0.35
Number of laser tracks, *N*	5

2.2. Thermal Properties

The thermal properties of solid 304L stainless steel are temperature-dependent and identified in Ref. [10]. These thermal properties include thermal conductivity, specific heat, and density. The thermal conductivity of the powder bed is defined by the following effective medium relationship:

$$k_p = k_s \frac{2\varphi\left(k_g - k_s\right) + k_g + 2k_s}{k_g + 2k_s + \varphi\left(k_s - k_g\right)} \tag{4}$$

where k_p, k_s and k_g are the thermal conductivity of the powder bed, solid material and air, respectively [11]. φ is the porosity of the powder bed, which can be expressed as:

$$\varphi = \frac{\rho_s - \rho_p}{\rho_s} \tag{5}$$

where ρ_s and ρ_p are the density of the solid and powder bed, respectively [12]. It is assumed in this paper the porosity is φ = 0.60 for the powder state. Figure 2 shows variations in the thermal conductivity, density and specific heat capacity of solid and powder 304L with temperature.

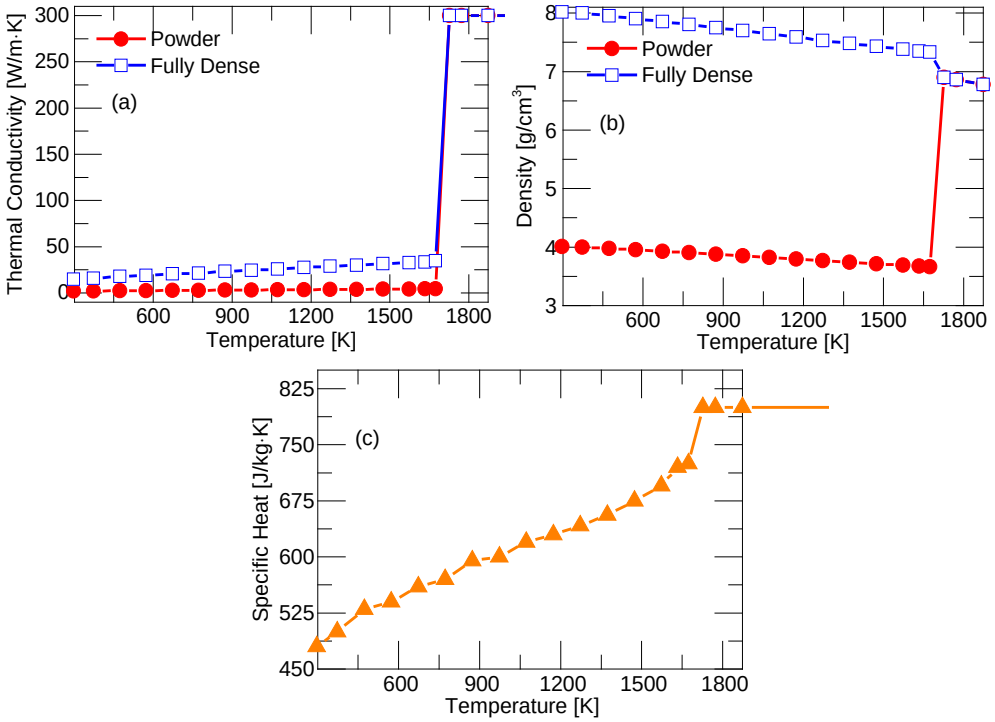

Fig. 2. Literature values for temperature dependent (a) thermal conductivity, (b) density, and (c) specific heat of 304L Stainless Steel [10].

Thermal conductivity is multiplied 10 times the normal thermal conductivity of solid 304L for temperatures greater than the melting point. The value of thermal conductivity multiplier was determined through fitting the model's predicted melt pool size to experimental results. This method of effective thermal conductivity of the melt pool is well established in literature and is used to simulate the increased heat transfer due to convection of the melt pool in conduction models [17].

Taking the melting and solidification phenomena during SLM into consideration, the latent heat of fusion should be not be neglected. The total enthalpy H is represented by:

$$H = \begin{cases} \int c_p dT, & T < T_s \\ \int c_p dT + \dfrac{T - T_s}{T_l - T_s} \cdot L, & T_s \le T \le T_l \\ \int c_p dT + L, & T > T_l \end{cases} \quad (6)$$

where L is the latent heat of fusion, c_p is the specific heat capacity, and T is the temperature, T_l and T_s are the liquidus and solidus temperature, respectively [13]. L is 261 kJ/kg, T_l is 1727 K, and T_s is 1673 K for 304L stainless steel [10].

3. Experimental Procedure

Model validation experiments involved building the 125 304L stainless steel samples with dimensions of 5x5x10 mm^3 displayed in Fig. 3. Samples were built with varied process parameters using a Renishaw AM250 SLM platform. The AM250 has a 200 W maximum fiber laser and contains a 250x250x300 mm^3 build volume. Process parameters used to build the samples include combinations of the laser powers, hatch spacing, and scan speeds listed in Table 2 and no rotation of the laser scan path between layers allowing easy identification of melt pool boundaries. Samples were removed from the build plate using Electrical Discharge Machining (EDM), mounted, polished, and electrolytically etched using 60/40 Nitric Acid. Experimental measurements were made in the cross section of samples for characterization of melt pool size. Experimental analysis included melt pool width and depth measurement with a Hirox KH-8700 optical microscope and microstructure characterization of the solidification structure, grain size, and cell spacing with a Hitachi S-4700 FESEM. Experimental measurements were completed to validate thermal model predictions of melt pool size, cooling rate, and solidification structure.

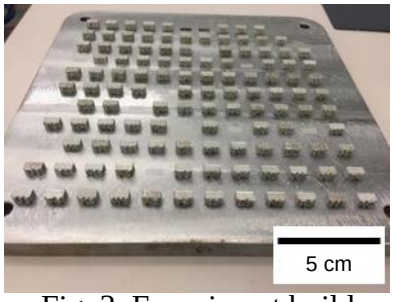

Fig. 3. Experiment build.

Table 2. Experiment Process Parameters.

Power [W]	Hatch Spacing [mm]	Scan Speed [mm/s]
120	0.045	615
140	0.065	715
160	0.085	800
180	0.105	875
200	0.125	940

4. Experimental and Simulation Results

4.1. Simulated Thermal History

Figure 4 (a) shows the temperature profile changes in the computed temperatures at various monitoring locations, points 1, 2, and 3 (middle points of first, third and fifth tracks) for a laser power of 120 W. Results indicate during the heating process the heating rate is very fast. During the cooling process, the cooling rate between the liquidus and solidus temperature is almost constant because of the release of the latent heat of fusion. Each point experiences several peak temperatures due to heat accumulation from subsequent laser tracks. The lower secondary peaks

correspond to the laser scanning the middle position on successive tracks. For example, there are three peak temperatures in Point 1, and the third peak temperature is lower than melting temperature. This means first track is affected by three tracks, but just re-melted by the second track.

Fig. 4 (b) shows the temperature profile changes as a function of distance in *z* direction at point 2 for three different laser powers when the simulation time is 3150 µs. The temperature slope of the distribution curve represents the temperature change becoming steeper as *z* increases, which indicates temperature gradient and cooling rate increase when distance into the model increases.

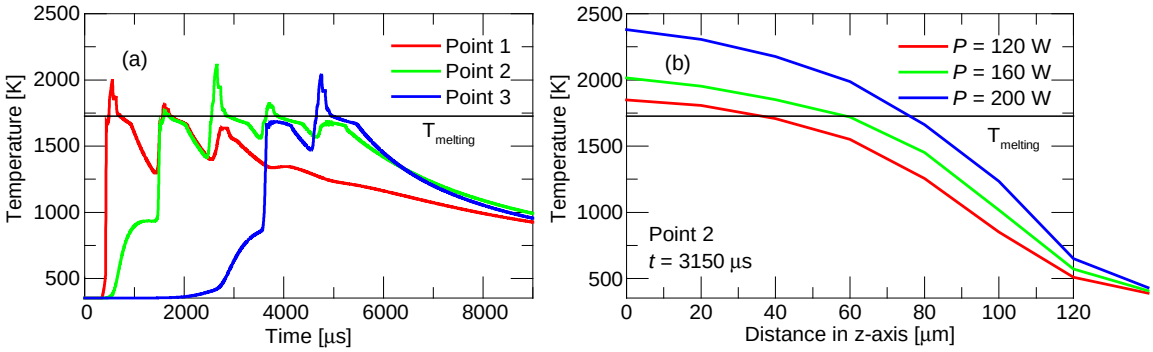

Fig. 4. (a) Thermal history of Points 1-3 for laser power of 120 W and (b) temperature distribution in *z*-direction for different laser powers for point 2 at t = 3150 µs.

4.2. Predicted Solidification Behavior

The temperature gradient, *G*, and cooling rate, *CR*, are calculated from the temperature field. Solidification rate, *R*, can be calculated by *CR* divided by *G*. The combined form of *G* and *R* is the solidification morphology factor *G/R*. The cooling rate can be directly related to the grain size in fusion zone. The morphology parameter can be used to describe the shape of solidification structures, such as (from high *G/R* value to low) planar, cellular, columnar, dendritic, and equiaxed dendritic [13].

The cooling rate of the FEA model was determined using:

$$CR = \left.\frac{dT}{dt}\right|_{T=T_{melting}} = \left|\frac{T_l - T_s}{t_l - t_s}\right| = G \times R \tag{7}$$

where *CR* is the cooling rate, T_l - T_s is the difference between the liquids and solidus temperatures, and t_l - t_s is the time interval between T_l and T_s.

The temperature gradient is evaluated at the liquidus temperature in the liquid interface, which can be calculated by:

$$G = \|\nabla T\| = \left.\sqrt{\left(\frac{\partial T}{\partial x}\right)^2 + \left(\frac{\partial T}{\partial y}\right)^2 + \left(\frac{\partial T}{\partial z}\right)^2}\right|_{T=T_l} \tag{8}$$

The solidification rate can be calculated by the cooling rate divided by the temperature gradient:

$$R = \frac{CR}{G} = \frac{(dT/dt)_{T=T_{melting}}}{G} \tag{9}$$

The calculation of the *CR* map and *G/R* map on the top surface of the powder bed and cross-section (A-A) has been studied in the following Fig. 5 (a-d) for *P*=120 W, *H*=65 µm, and *SS*=715 mm/s. Laser power is continuously added to next track during the multi-track laser melting. The associated additions of energy to the powder bed change its melt pool size and alter its temperature distributions. These solidification parameters are higher at the edge of the melt pool than in the center. This trend is very noticeable in the *G/R* distribution (Fig. 5 (b)). Meanwhile, the magnitude of the *CR* and *G/R* near the maximum depth of the melt pool is much higher than at the melt pool surface.

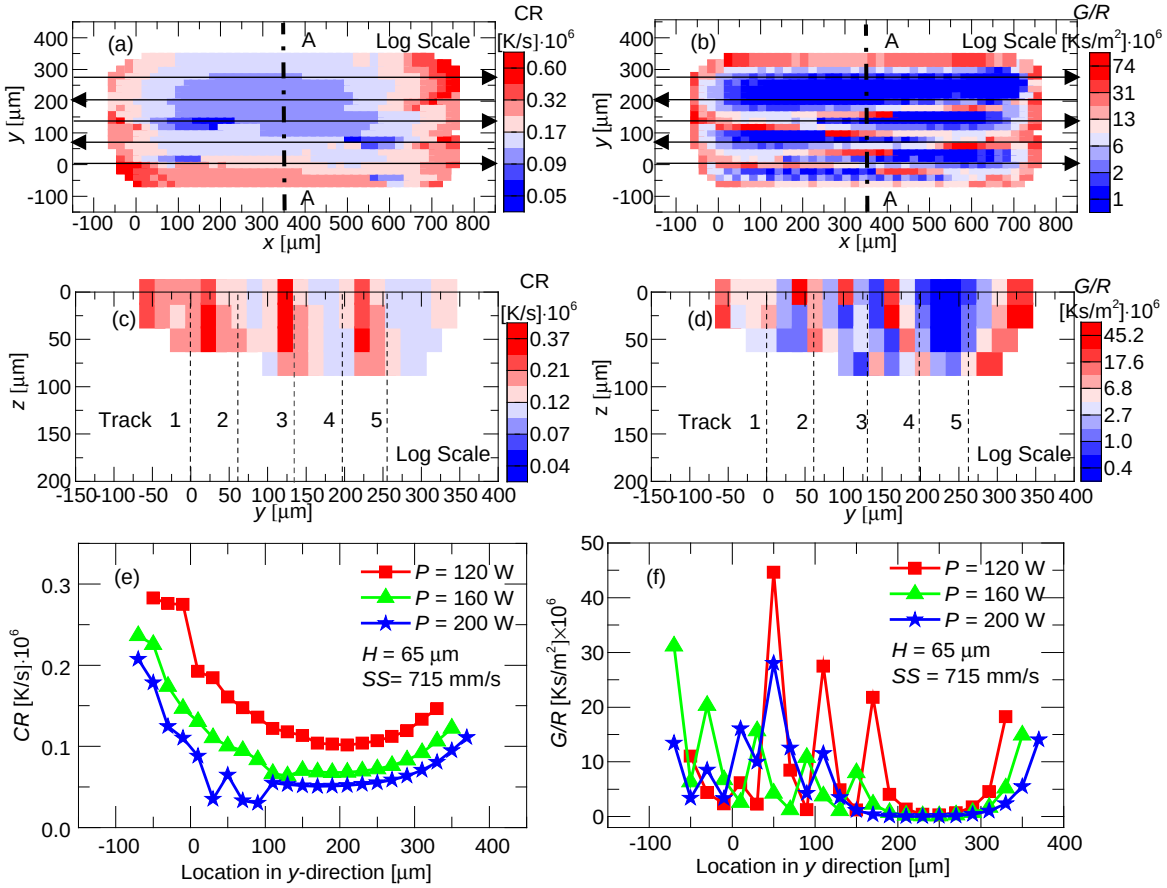

Fig. 5. (a) Cooling Rate and (b) Solidification Morphology Factor map for the model top surface. (c) Cooling Rate and (d) Solidification Morphology Factor map for the model cross-section. (e) Cooling Rate and (f) Solidification Morphology Factor across laser tracks for laser powers of 120, 160, and 200 W.

The dependence of *CR* and *G/R* on the top surface of powder bed's cross section at three different powers has been studied in Fig. 5 (e) and (f). As expected, *CR* increases with decreasing laser power and increases from laser center to the edge. Results in Fig. 5 (e) also show an

invariance in the cooling rate across laser tracks develops after a certain number of tracks. It is expected that this invariance would continue if more tracks were simulated. The predicted invariance in cooling rate makes sense and is confirmed through an observation of constant solidification structure across laser tracks in experimental findings discussed later. It should also be noted that *G/R* increases from laser center to edge and maximum value of *G/R* is predicted at the melt pool edge.

The effect of solute and thermal gradients on the solidification front can be described by the concept of constitutional super-cooling criterion, which is mathematically stated as:

$$G / R \geq \Delta T_E / D_L, \ \textit{for plane front solidification}$$
$$G / R \leq \Delta T_E / D_L, \ \textit{for cellular or dentritic solidification} \quad (10)$$

where ΔT_E is the equilibrium solidification temperature range (T_l-T_s) and D_L is the solute diffusion coefficient [14]. The value of ΔT_E for 304L stainless steel is 54 K and D_L is the diffusion coefficient of chromium in liquid iron and is $5 \cdot 10^{-9}$ m^2/s. Therefore, $\Delta T_E / D_L = 54/5 \cdot 10^{-9} = 1.04 \cdot 10^{10}$ $K \cdot s/m^2$, from the criterion. Solidification will be cellular or dendrite for values of *G/R* less than or equal to $1.04 \cdot 10^{10}$ $K \cdot s/m^2$. The maximum simulated value of *G/R* is $74 \cdot 10^6$ $K \cdot s/m^2$. This means the predicted value of *G/R* is much less than $\Delta T_E / D_L$; therefore, the model predicts cellular/dendritic solidification in the entire melted domain.

4.3. Experimental Melt Pool Size

Fig. 6 (a) shows the definition of simulated melt pool half width and depth. These dimensions are defined by the maximum dimension the simulated temperature reached greater than the melting temperature of 304L stainless steel. Fig. 6 (b) shows the definition of experimental melt pool half width and depth defined by the visible laser track boundary.

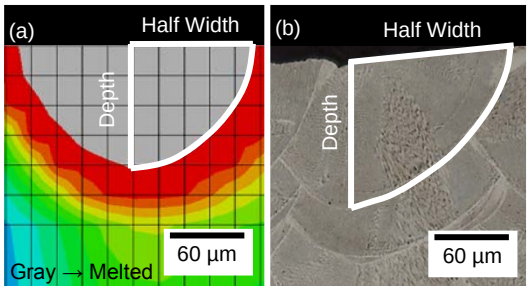

Fig. 6. Definition of melt pool half width and depth in (a) simulation and (b) experiment.

Fig. 7 (a-h) contains experimental melt pool measurements as a function of laser power, scan speed, and hatch spacing. Results in these figures show melt pool size increases with increasing laser power and decreasing scan speed as expected in samples built with lower hatch spacing (45 µm -85 µm). However, in a wider hatch spacing of 105 µm, melt pool size follows no clear increasing trend with increasing laser power and decreasing scan speed. This result is explained by the wider hatch spacing causing less heat buildup from subsequent laser tracks; therefore, melt pools behave similar to single tracks.

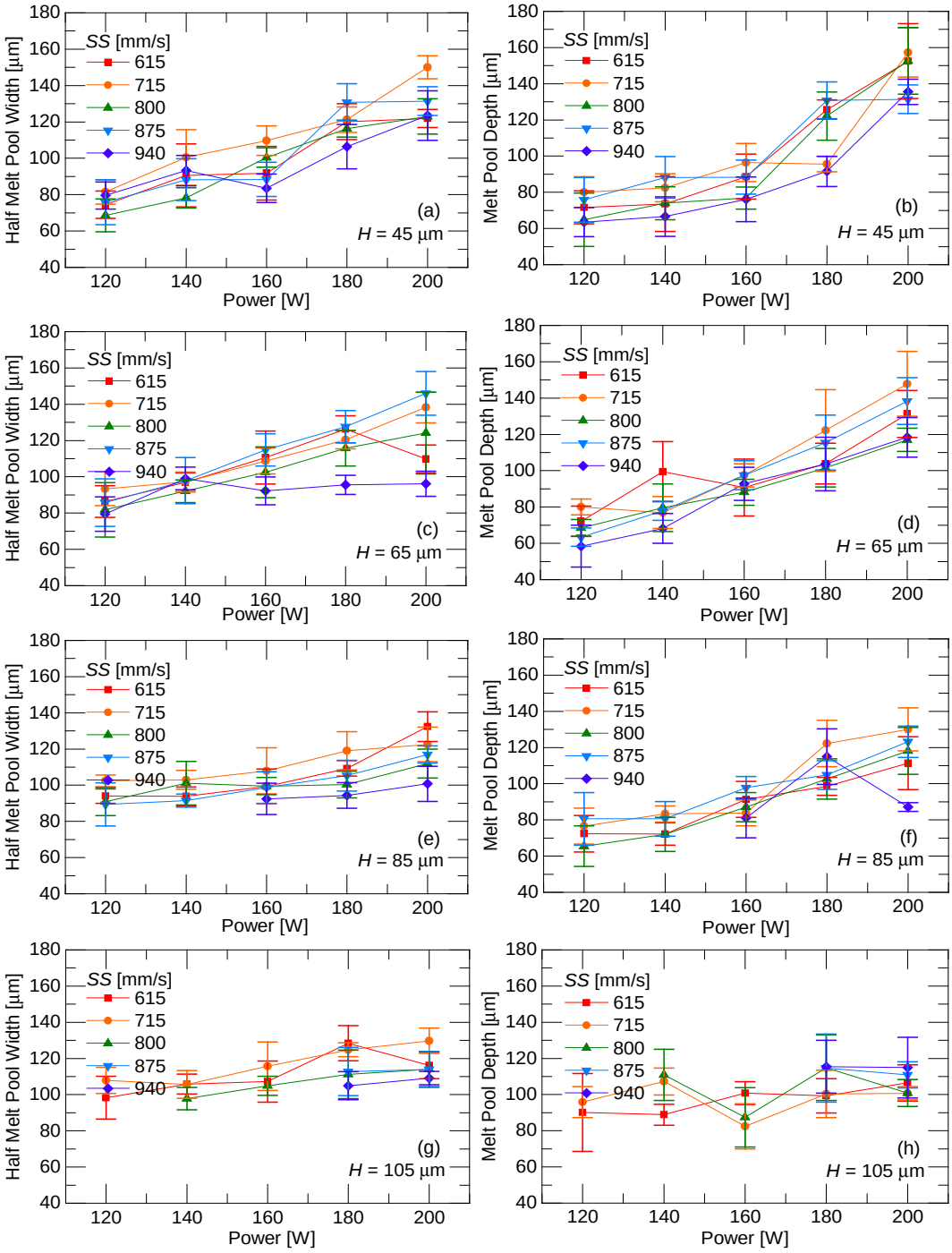

Fig. 7. Melt pool size as a function of laser power and scan speed including (a) half width for hatch spacing of 45 µm, (b) depth for hatch spacing of 45 µm, (c) half width for hatch spacing of 65 µm, (d) depth for hatch spacing of 65 µm, (e) half width for hatch spacing of 85 µm, (f) depth for hatch spacing of 85 µm, (g) half width for hatch spacing of 105 µm, and (h) depth for hatch spacing of 105 µm.

4.4. Model Melt Pool Size Prediction Validation

Comparison of melt pool sizes is displayed in Fig. 8 and 9 between experimental and simulation values as a function of laser power at hatch spacing of 65 µm and 105 µm when the scan speed is 715 mm/s. Results in these figures show melt pool size increases with higher laser power and lower hatch spacing. The simulated melt pool sizes are in good agreement with experimental results, especially melt pool width, which can be seen in Fig. 8 (a) and Fig. 9 (a). In these figures the maximum error between simulation and experimental melt pool width is 4% and 8%, respectively. It can also be concluded from these figures laser power is the determining parameter affecting melt pool sizes when compared to hatch spacing.

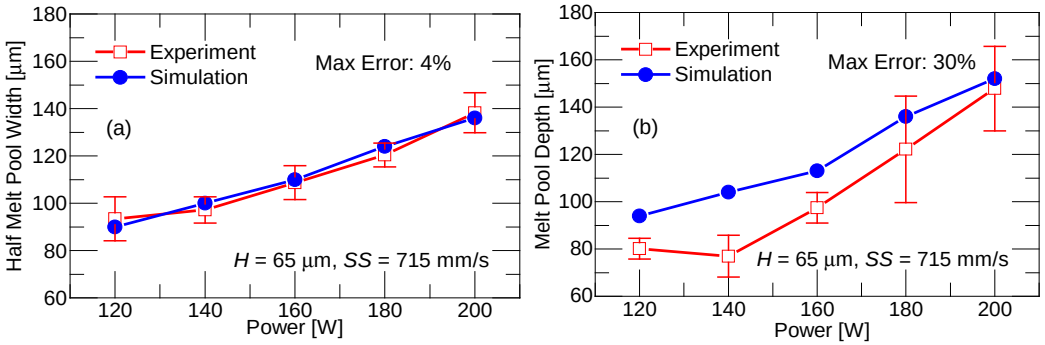

Fig. 8. Experiment vs. simulation (a) half melt pool width and (b) melt pool depth as a function of laser power for hatch spacing of 65 µm and scan speed of 715 mm/s.

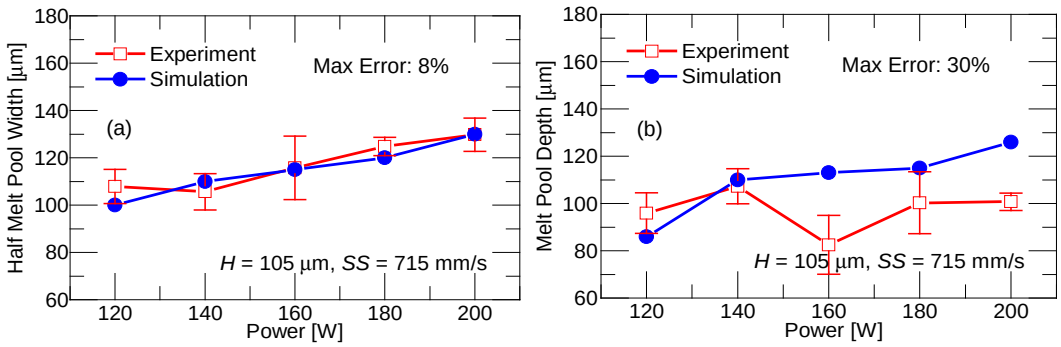

Fig. 9. Experiment vs. simulation (a) half melt pool width and (b) melt pool depth as a function of laser power for hatch spacing of 105 µm and scan speed of 715 mm/s.

4.5. Experimental Microstructure

Figure 10 contains optical micrographs at different magnifications of a 304L stainless steel sample built with a laser power of 180 W, hatch spacing of 65 µm, and a scan speed of 940 mm/s. These figure display the cellular grain structure of the sample. The austenitic phase of the sample is also highlighted in the figure through the dark gray shade. The result of cellular grain structure and austenitic phase seen in this sample was consistent throughout built samples.

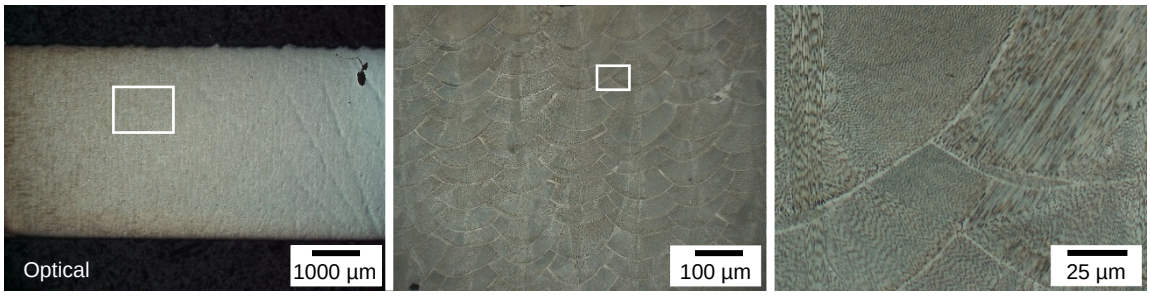

Fig. 10. Optical micrographs of sample built with laser power of 180 W, hatch spacing of 65 µm, and scan speed of 940 mm/s.

The cellular grain structure seen in these optical micrographs and further identified by SEM (Fig. 13) confirms the thermal model predictions of a cellular/dendritic solidification structure. This confirmation validates the continuum thermal model and solidification parameter calculation approach used in this work to predict microstructure.

Average grain size in samples was measured following procedures outlined in ASTM E1382-97 [18]. This standard was used to measure grain size in samples built with hatch spacing from 0.045-0.105 mm and powers from 120-200 W. Figure 11 contains the results of the average grain size in samples as a function of hatch spacing and laser power. Results in the figure show average grain size increases with laser power. Grain size increases with increasing laser power because more energy input into the melting process from higher laser powers leads to a decrease in the cooling rate. Grain size correlates to cooling rate, with larger grain sizes resulting from slower cooling rates. Therefore, the lower cooling rates in higher laser powers result in larger grain sizes. This result qualitatively matches well with thermal model predictions in Fig. 5 (e) of lower cooling rates in higher laser powers.

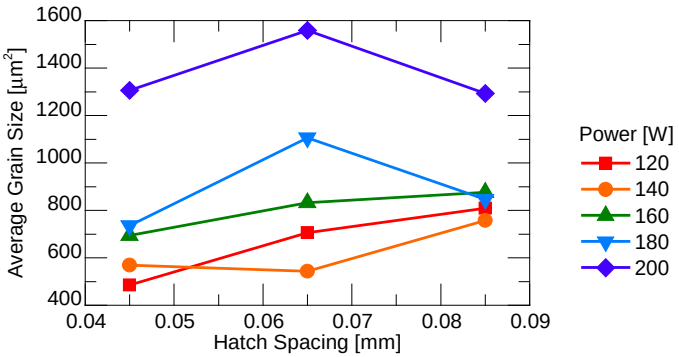

Fig. 11. Average grain size as a function of hatch spacing and laser power.

In order to quantitatively correlate thermal model cooling rate predictions with experimental cooling rates cell spacing was measured in samples. The relationship found in [16] between cell spacing and cooling rate in stainless steel is given by:

$$\lambda = 80 \cdot CR^{-0.33} \tag{11}$$

where λ is the cell spacing and CR is the cooling rate. Fig. 12 (a) shows the cellular microstructure in a 304L sample and (b) shows the definition of cell spacing, λ, in a high magnification image, which is used in Eq. 11 to estimate the cooling rate.

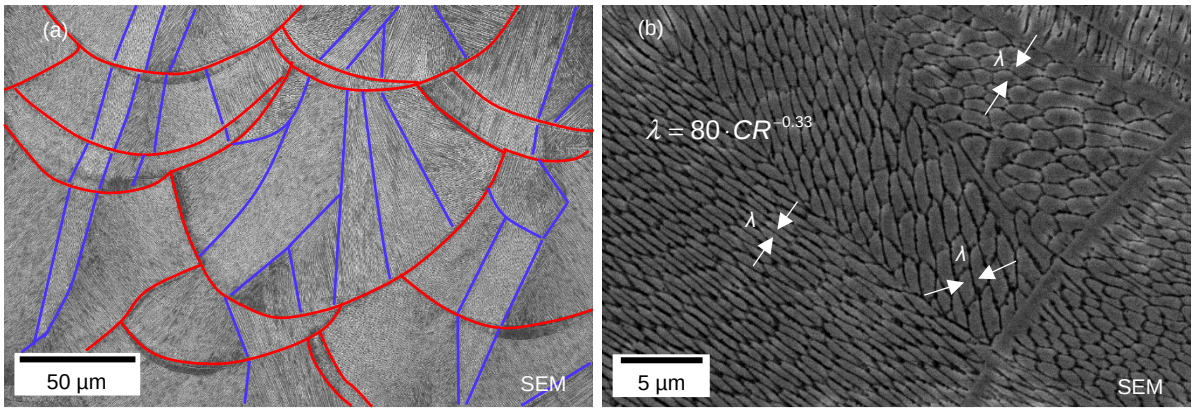

Fig. 12. (a) SEM image of 304L sample showing cellular grain structure with track boundaries highlighted in red and grain boundaries in blue and (b) high magnification SEM image of 304L sample showing definition of cell spacing, λ.

Several cell spacing measurements were taken within samples and averaged together in order to calculate the average cooling rate. Cell spacing measurements in all analyzed samples resulted in calculated cooling rates on the order of magnitude of ~10^5 to ~10^6 K/s. This experimental cooling rate result is common in SLM and matches well with the thermal model predictions of cooling rates on the order of ~10^5 K/s (Fig. 5).

Experimental microstructure analysis has shown the continuum thermal model developed in this paper successfully predicted the observed cellular solidification structure. The experiment has also confirmed the model captures the appropriate trend of lower cooling rates in samples built with higher laser powers through grain size analysis. Cell spacing measurement has shown the experimental order of magnitude for cooling rate agrees with thermal model predictions of ~10^5 K/s.

5. Discussion of Results and Conclusions

A numerical model and experimental study was developed to study the effect of laser process parameters on thermal history, melt pool size and microstructure formation during SLM process using 304L stainless steel. The simulated results and the experimental results consistent with each other very well. The main results are concluded as following:

1. Continuum model correctly predicts melt pool size and trends including melt pool size increase with laser power and lower scan speed.

2. Experimental melt pool sizes followed no clear trends in higher hatch spacing because the spacing is wide enough to promote a near single track scan mode.

3. Experiments determined grain size increased with increasing laser power. The thermal model predicts lower cooling rates for higher laser powers which correlates to the experimental findings.

4. Simulation and experiments showed cooling rate varied in melted material with cooling rate estimated to range from ~10^5 to ~10^6 K/s in analyzed samples. Simulation solidification parameter calculation approach validated through correctly predicting cellular structure

6. Acknowledgements

This work was funded by Honeywell Federal Manufacturing & Technologies under Contract No. DE-NA0002839 with the U.S. Department of Energy. The United States Government retains and the publisher, by accepting the article for publication, acknowledges that the United States Government retains a nonexclusive, paid up, irrevocable, world-wide license to publish or reproduce the published form of this manuscript, or allow others to do so, for the United States Government purposes. This work was also supported by the National Science Foundation (EEC-1461102).

7. References

1. Patil, R. B. and Yadava, V., 2007, "Finite element analysis of temperature distribution in single metallic powder layer during metal laser sintering," Int. J. Mach. Tools Manuf., 47(7–8), pp. 1069–1080.
2. Gusarov, A. V., Yadroitsev, I., Bertrand, P., and Smurov, I., 2007, "Heat transfer modeling and stability analysis of selective laser melting," Appl. Surf. Sci., 254, pp. 975–979.
3. Gusarov, A.V. and Smurov, I., 2009, "Two-dimensional numerical modeling of radiation transfer in powder beds at selective laser melting," Appl. Surf. Sci., 255, pp. 5595–5599.
4. Gusarov, A.V. and Smurov, I., 2010, "Modeling the interaction of laser radiation with powder bed at selective laser melting," Phys. Proc., 5, pp. 381–394.
5. Masmoudi, A., Bolot, R., and Coddet, C., 2015, "Investigation of the laser–powder–atmosphere interaction zone during the selective laser melting process," J. of Mat. Proc. Tech., 225, pp. 122–132.
6. Loh, L. E., Liu, Z. H., Zhang, D. Q., Mapar, M., Sing, S. L., Chua, C. K., and Yeong, W. Y., 2014, "Selective Laser Melting of aluminum alloy using a uniform beam profile," Virt. and Phys. Proto., 9(1), pp. 11–16.
7. Antony, K., Arivazhagan, N., and Senthilkumaran, K., 2014, "Numerical and experimental investigations on laser melting of stainless steel 316L metal powders," J. of Man. Proc., 16(3), pp. 345–355.
8. Kolossov, S., Boillat, E., Glardon, R., Fischer, P., and Locher, M., 2004, "3D FE simulation for temperature evolution in the selective laser sintering process," Int. J. Mach. Tools Manuf., 44(2–3), pp. 117–123.
9. Parry, L., Ashcroft, I.A., and Wildman, R.D., 2016, "Understanding the effect of laser scan strategy on residual stress in selective laser melting through thermo-mechanical simulation," Add. Man. A, 12, pp. 1–15.
10. Mills, K. C., 2002, *Recommended Values of Thermophysical Properties for Selected Commercial Alloys*, Woodhead Publishing.

11. Levy, O. and Stroud, D., 1997, “Maxwell Garnett theory for mixtures of anisotropic inclusions: Application to conducting polymers,” Phys. Rev. B, 56, pp. 8035–8046.
12. Hussein, A., Hao, L., Yan, C., and Everson, R., 2013, “Finite element simulation of the temperature and stress fields in single layers built without-support in selective laser melting,” Mat. Des., 52, pp. 638–647.
13. Zhang, W., Roy, G. G., Elmer, J. W., and Debroy, T., 2003, “Modeling of heat transfer and fluid flow during gas tungsten arc spot welding of low carbon steel,” J. of App. Phys., 93, pp. 3022–3033.
14. Hu, H., Ding, X., and Wang, L., 2016, “Numerical analysis of heat transfer during multi-layer selective laser melting of AlSi10Mg,” Int. J. for Light and Elect. Opt., 127(20), pp. 8883–8891.
15. Debroy, T. and David, S. A., 1995, “Physical processes in fusion welding,” Rev. Mod. Phys., 67, pp. 85–112.
16. Elmer, J. W., Allen, S. M., and Eagar, T. W., 1989, “Microstructural development during solidification of stainless steel alloys,” Met. Tran. A, 20, pp. 2117–2131.
17. Ladani, L., Romano, J., Brindley, W., and Burlatsky, S., 2017, “Effective liquid conductivity for improved simulation of thermal transport in laser beam melting powder bed technology,” Add. Man., 14, pp. 13–23.
18. ASTM E1382–97 Standard Test Methods for Determining Average Grain Size Using Semiautomatic and Automatic Image Analysis, ASTM International, West Conshohocken, PA, 2015.